

# Automatic 3D reconstruction of an anatomically correct upper airway from endoscopic long range OCT images

ZHIJIAN ZHUANG,<sup>1,2,3,4,†</sup> DELANG CHEN,<sup>1,2,3,†</sup> ZHICHAO LIANG,<sup>1,2,3</sup>  
SHUANGYANG ZHANG,<sup>1,2,3</sup> ZHENYANG LIU,<sup>1,2,3</sup> WUFAN CHEN,<sup>1,2,3</sup>  
AND LI QI<sup>1,2,3,\*</sup>

<sup>1</sup>School of Biomedical Engineering, Southern Medical University, 1023 Shatai Rd., Baiyun District, Guangzhou, Guangdong, 510515, China

<sup>2</sup>Guangdong Provincial Key Laboratory of Medical Image Processing, Southern Medical University, 1023 Shatai Rd., Baiyun District, Guangzhou, Guangdong, 510515, China

<sup>3</sup>Guangdong Province Engineering Laboratory for Medical Imaging and Diagnostic Technology, Southern Medical University, 1023 Shatai Rd., Baiyun District, Guangzhou, Guangdong, 510515, China

<sup>4</sup>The Third People's Hospital of Zhuhai, 166 Hezheng Rd., Xiangzhou District, Zhuhai, Guangdong, 519000, China

<sup>†</sup>These authors contributed equally to this work

\*qili@smu.edu.cn

**Abstract:** Endoscopic airway optical coherence tomography (OCT) is a non-invasive and high resolution imaging modality for the diagnosis and analysis of airway-related diseases. During OCT imaging of the upper airway, in order to reliably characterize its 3D structure, there is a need to automatically detect the airway lumen contour, correct rotational distortion and perform 3D airway reconstruction. Based on a long-range endoscopic OCT imaging system equipped with a magnetic tracker, we present a fully automatic framework to reconstruct the 3D upper airway model with correct bending anatomy. Our method includes an automatic segmentation method for the upper airway based on dynamic programming algorithm, an automatic initial rotation angle error correction method for the detected 2D airway lumen contour, and an anatomic bending method combined with the centerline detected from the magnetically tracked imaging probe. The proposed automatic reconstruction framework is validated on experimental datasets acquired from two healthy adults. The result shows that the proposed framework allows the full automation of 3D airway reconstruction from OCT images and thus reveals its potential to improve analysis efficiency of endoscopic OCT images.

© 2023 Optica Publishing Group under the terms of the [Optica Open Access Publishing Agreement](#)

## 1. Introduction

Endoscopic optical coherence tomography (OCT) [1] is developing rapidly in recent years. It is a high-resolution, non-ionizing, label free, and cross-sectional imaging modality that has been used for disease screening of luminal biological tissues such as coronary arteries [2,4], gastrointestinal tract [5,6], and airway [7–9]. For the imaging of the airway, endoscopic airway OCT imaging aims to detect the subsurface structure of the airway, where abnormalities due to chemical stimuli or toxic substances can result in airway tissue deformation, cysts and even necrosis [10–13]. In the process of imaging the upper airway, the fiber optic probe performs a helical scan by pulling back the probe linearly along the path from the hypopharynx to the nostril and using optical fiber for data transmission to obtain the detailed structure of the upper airway.

A conventional endoscopic OCT system is consisted of an optical interferometer, scanning mechanics, and signal processing electronics. The sample arm of the interferometer includes a fiber optic probe that focuses and scans the light beam on airway tissue. During the scanning and pullback operation, the spatial location of the probe is unknown, and therefore the anatomical

bending structure of the upper airway is missing. To achieve a complete and anatomically correct 3D model of the upper airway, it is crucial to collect information about the centerline of the upper airway. Due to the particular anatomical structure of the human upper airway, Jing et al. [14] proposed a novel endoscopic long range optical coherence tomography (LR-OCT) system equipped with a magnetic sensor and position tracker. As shown in Fig. 1, the system has an imaging probe integrated with a magnetic sensor for imaging the upper airway. A magnetic field generator located outside the human body provides the spatial position information of the sensor and therefore a scanning trajectory of the imaging probe can be obtained during imaging. This LR-OCT system enables complete and anatomically correct imaging of the upper airway.

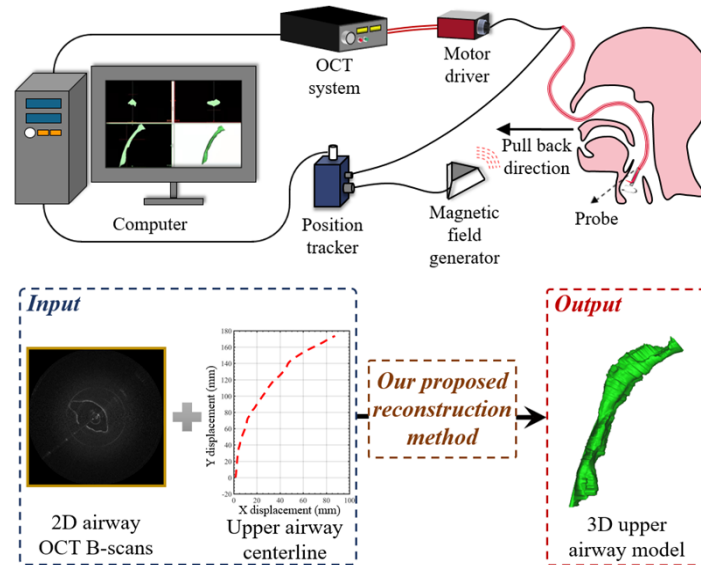


**Fig. 1.** Upper panel: the schematic of OCT system equipped with a magnetically tracked imaging probe. Lower panel: the proposed airway reconstruction method takes raw OCT images and the airway centerline as input, and outputs a 3D airway model with correct bending anatomy.

Despite the use of the above endoscopic OCT system with magnetically tracked probe, achieving an anatomically correct reconstruction of the upper airway remains a challenging task. This is mainly due to difficulties in the image post-processing procedures, which can be divided into the following steps: 1) airway lumen contour segmentation, 2) non-uniform rotation error correction, and 3) anatomic bending operation. Currently, these processing steps are performed separately and are heavily relied on manual intervention. Since an OCT image dataset contains hundreds to thousands of images, processing these images can be highly time-consuming. Additionally, subjective differences between observers also influence the accuracy of the results. Therefore, a comprehensive processing framework that integrates these procedures are highly desired for efficient reconstruction of the 3D airway structure.

Computerized algorithms have been proposed for the above airway OCT processing procedures to facilitate efficient analysis. Firstly, for airway lumen segmentation, the goal is to detect and extract the airway lumen contour. To achieve this, mathematical model-based methods such as active contours [15–18], sparse higher-order potentials [19], and A-scan methods [20,21] have been proposed. Other than these methods, graph-theory-based techniques such as the dynamic programming (DP) algorithm [22,23] has been shown to be able to preserve the continuity of the lumen contour, and thus has been used in multiple endoscopic OCT imaging applications.

Second, except for tissue segmentation, another important processing step is the correction of initial rotation angle error, or IRAE. Because the imaging catheter cannot maintain a stable rotation rate during airway imaging, the starting angle of each B-scan image is slightly drifting. This error of the initial rotation angle results in twisted airway reconstruction and therefore has to be corrected. To correct for IRAE, one solution is the use of sheath markers, as seen in gastrointestinal balloon catheter OCT systems [24]. However, balloon catheters are not suitable for airway imaging and markers may obstruct the field of view. Zhuang et al. recently proposed a method [25] for performing automatic IRAE correction. This method estimates the initial rotation angle for each frame by calculating the similarity between the lumen contours of adjacent frames through a graph searching algorithm. It then applies the initial angle to each frame to compensate for the IRAE.

Thirdly, for anatomic bending, although curved structure reconstruction is used for coronary arteries OCT [26], there is currently no widely acceptable method for upper airway reconstruction. By incorporating the magnetically tracked imaging probe, previous research [27–29] has been shown that the anatomic bending can be done by tracing the tracked probe trajectory manually.

Our proposed reconstruction method is aimed at providing a comprehensive and efficient analysis tool for generating anatomically correct 3D model of the human upper airway from airway OCT images. Our method integrate segmentation, IRAE correction, and anatomic bending into a sequentially processing framework. We also propose an adaptive airway lumen detection algorithm based on the dynamic programming algorithm to enhance the quality of the final 3D reconstructed airway model. By combining the processed contours with recorded anatomical centerline information, our algorithm is able to produce complete and correct 3D model of the human upper airway. The contributions of our work are summarized as follows:

- 1) Our work is the first fully automatic airway OCT processing framework that combines tissue segmentation, image correction, and anatomic bending to reconstruct 3D upper airway structure;
- 2) We optimized the DP method used in the segmentation step to improve the accuracy and robustness of airway lumen contour detection in OCT images;
- 3) Tested in two human dataset, our method achieves accurate reconstruction of the upper airway with much less time cost compared to previous methods.

## 2. Methods

### 2.1. Algorithm overview

As shown in Fig. 2, our method is consisted of three primary steps: segmentation, IRAE correction, and anatomic bending. The segmentation step is to accurately identify the airway lumen contour based on an adaptive DP algorithm. Then, the IRAE correction step is performed for the detected lumen contour in each frame using a previously proposed method [25]. Finally, the anatomic bending step applies the magnetically tracked airway centerline and generates a 3D model of the airway.

### 2.2. Segmentation

Airway OCT image has some distinct features that can interfere with the identification of the airway lumen contour in the image. These features include oversaturated pixels caused by back reflection of the upper airway structure, speckle noise caused by high scattering of biological tissue, and mirror artifacts caused by phase modulation, among others. Additionally, the plastic sheath used to protect the imaging probe is also an artifact in the image that prevents the accurate delineation of airway lumen contour. When the plastic sheath touches the tissue surface, it becomes even more difficult to identify tissue boundary.

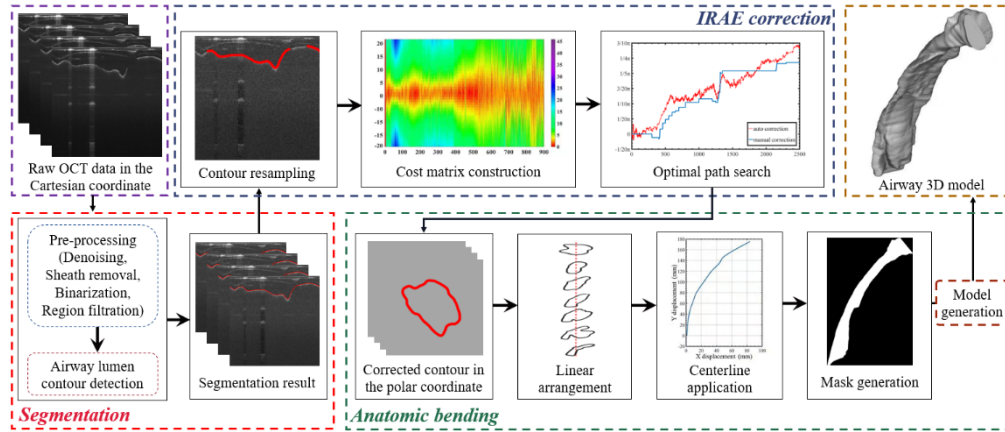


Fig. 2. The flowchart of our proposed method.

The goal of segmentation is to accurately detect and extract the airway lumen contour from a set of Cartesian airway OCT B-scans. Previously, a number of methods have been proposed for the automatic delineation of tissue contours in OCT images [30–32]. Among these methods, the graph-based DP algorithm has been a stable method validated in multiple researches [22,23]. The DP method is a graph search algorithm, and its result is a continuity path. This makes it well-suited for obtaining an optimal curve that describes the airway lumen contour.

Despite for the above advantage, in the original DP-based airway segmentation method, we encounter two main problems. Firstly, the segmentation results are vulnerable to sheath artifacts, resulting in segmentation offset as shown in Fig. 3(g). Secondly, conventional DP typically misidentifies image areas contaminated by speckle noise or over-saturated A-lines [e.g., yellow boxes of Fig. 3(e)] as possible regions of normal airway lumen structures. This error leads to abnormal segmentation results, as shown in Fig. 3. (h).

To address these two issues, we propose to introduce a sheath removal step and an adaptive region filtration step as pre-processing procedures before contour detection. As we will show in our experiment, these two operations significantly improve the robustness of the original DP algorithm. For convenience, we named this improved algorithm Region-Adaptive DP (RADP) method.

The pre-processing step of the proposed RADP is composed of the following steps:

- 1) Image filtering. A median filter and an average filter are applied to the image, and then the pixel intensity is reassigned according to the following equation [33]:

$$I_x = I_M - I_A - I_B, \quad (1)$$

where  $I_x$  is the reassigned intensity of the pixel,  $I_M$  is the initial intensity of the pixel,  $I_A$  is the average intensity of corresponding A-line of the pixel,  $I_B$  is the average intensity of corresponding B-scan of the pixel. This step is aimed at removing high intensity noise and enhancing image contrast so as to help enhance the accuracy of the subsequent processing steps.

- 2) Sheath removal. To enhance the accuracy of airway lumen contour detection, it is important to address the issue of sheath artifacts that can significantly affect the results. The sheath is transversely distributed across the top region of the image. It has higher intensity than tissue because it is closer to the probe. Because the position of the sheath is within a certain range, we employ the DP algorithm within a determined z-range to detect the lower

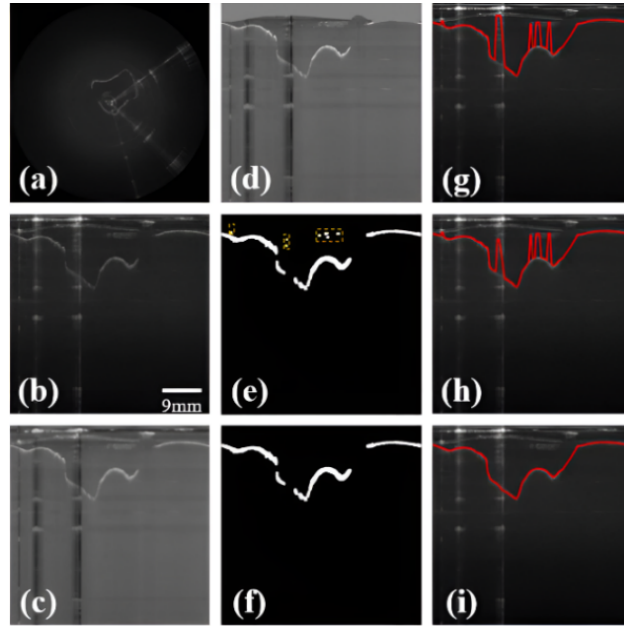


**Fig. 3.** The intermediate results of different steps of our segmentation approach: (a) OCT raw data; (b) Coordinate transformation; (c) Image filtering; (d) Sheath removal; (e) Otsu thresholding; (f) Adaptive region filtration; (g) The result of conventional DP without sheath removal; (h) The result of conventional DP by adding the sheath removal operation; (i) The result of our RADP.

edge of the sheath. We then set the image content above the detected edge to the mean intensity value of the whole image to remove all the sheath content. The result is as shown in Fig. 3(d).

- 3) Binarization. The sheath-removed image is transformed into a binary format, which is accomplished by applying a custom image intensity threshold.
- 4) Adaptive region filtration. To address the isolated region issue shown in Fig. 3(e), we classified these regions into two categories based on their characteristics. The regions that have a connected region size smaller than the custom threshold  $q$  are defined as region **A**, while the regions that overlap with other regions on the x-axis and are located above them are defined as region **B**. To implement adaptive region filtration, we record and number each connected region in the binary image, and a total of  $n$  regions are recorded. These regions are assigned the weighting function  $W$  [34], which is defined as follows:

$$W = \begin{cases} 0 & \text{if } s \in \mathbf{A} \text{ or } s \in \mathbf{B} \\ 1 & \text{otherwise} \end{cases} \quad (2)$$

The regions with  $W = 1$  are considered as the targeted regions. Next, to detect the airway lumen contour, we then identify the upper edge of each targeted region by using the DP algorithm [35]. Finally, as shown in Fig. 3(f), since there will be gaps between different regions, we fill these gaps through interpolation based on the detected upper edge. The interpolated edge is then smoothed to form a continuous curve, which represents our final detection result.



### 2.3. IRAE correction

We use an IRAE correction method proposed by our group previously [25]. It takes the detected airway lumen contour as input and calculates a rotational offset for each B-scans. Briefly, the correction procedure consists of the following steps: First, the detected airway lumen contour is resampled based on the chosen resampling rate to correct the shape error between the contour of each B-scans. Next, the resampled contour is compared with adjacent contours rotated for different angles to measure their similarity, which is used to construct a cost matrix. Then, DP is employed to search for the optimal path that represents the IRAE drifting in the cost matrix. Finally, we perform rotation angle estimation based on the traced rotational offsets.

### 2.4. Anatomic bending

The anatomic bending operation is aimed at correctly restoring the curved anatomical structure of the upper airway using the processed airway contours and the magnetically tracked airway centerline as inputs. During the imaging process of the upper airway, the magnetic sensor simultaneously records 1) the distance between the cross-sectional plane and the starting point of the path, and 2) the angle between the corresponding plane and the horizontal plane. The data is combined in the position tracker to obtain the centerline of the upper airway.

Figure 4 shows the anatomic bending and airway 3D model reconstruction process. We convert the corrected 2D contour to 3D space by utilizing the curvature information of the centerline captured by the position tracker. This enables us to position the contour at the corresponding centerline location. The specific process for anatomic bending is as follows:

- 1) Linear arrangement. The IRAE corrected contours are evenly distributed along a straight line in the z-axis of the 3D space, as shown in Fig. 4(b). The length of the straight line corresponds to the number of images in the OCT dataset times the pullback resolution.
- 2) Centerline application. After obtaining the centerline, we interpolate the curve to let its length equal to that of the straight line. In this way, we can evenly distribute the airway contours along the centerline curve. As shown in Fig. 4(d), we place the contour onto the centerline such that the plane of each contour is perpendicular to the centerline.
- 3) Mask generation. Each contour placed on the curve is first filled with ones to generate a corresponding mask. However, since the angle between the contour plane and the horizontal plane varies, there will be gaps between adjacent contours and their corresponding masks. To fill these gaps, we apply dilation and erosion operations to each mask such that a 3D mask is obtained. Based on the projection length of the curve along the z-axis, we extract a 2D horizontal mask from the 3D mask every unit length along the z-axis. The resulting masks are as shown in Fig. 4(e).
- 4) Model generation. The 2D horizontal masks are transferred to Mimics (Materialise, Leuven, Belgium) to obtain a 3D solid model of the upper airway, as shown in the final model in Fig. 4(f).

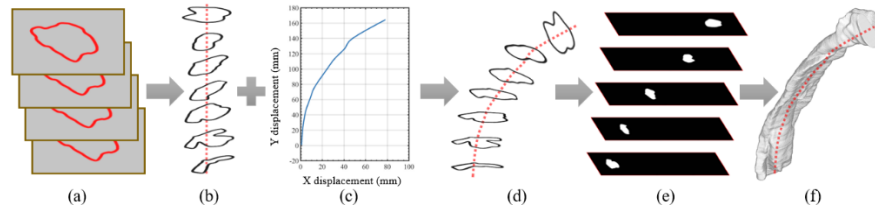


**Fig. 4.** Schematic diagram of bending correction principle. (a)~(f) represent the intermediate results of different steps of our anatomic bending approach: (a) The IRAE corrected contours; (b) Linear arrangement; (c) The upper airway centerline; (d) Centerline application; (e) Mask generation; (f) Model generation.

### 3. Experimental setup

#### 3.1. Upper airway OCT image datasets

We assessed the feasibility of our proposed framework using two sets of adult airway data acquired separately from two different types of LR-OCT systems [14,36]. These LR-OCT systems employ light sources with longer coherence lengths than previous endoscopic OCT systems, thereby significantly extending the imaging range without compromising resolution. With this extended imaging range, the LR-OCT systems can image adult airways with internal diameters that exceed the typical OCT axial imaging range. The two subjects in our study were healthy and met the testing criteria, and we obtained a single dataset from each subject, whose basic information is presented in Table 1. This study was approved by Southern Medical University and carried out in compliance with institutional guidelines. Table 1 provides basic information about the datasets.

**Table 1. Datasets used in the experiments**

Dataset	Dataset size	Imaging range	Axial resolution in tissue	Imaging rate during pullback
Dataset1	$512 \times 512 \times 300$	45 mm	9 $\mu\text{m}$	10 frames/mm
Dataset2	$512 \times 512 \times 900$	30 mm	6 $\mu\text{m}$	10 frames/mm

#### 3.2. Manual segmentation

Manual segmentation was performed by two experienced annotators using the following steps: 1) mark a series of feature points (generally no more than 50) on the edge of the upper airway lumen. The interval between the marked points decreased as the rate of change of the slope of the edge curve increased; 2) interpolate these points to obtain an initial lumen contour; 3) modify the position of the marked points to further refine the contour until the annotator is satisfied. The mean coordinates of the labeled contours by the two annotators were calculated to obtain the final results.

#### 3.3. Evaluation metrics

To measure the accuracy of our RADP method, we utilized three evaluation metrics: mean absolute difference (MAD), root mean squared error (RMSE), and dice similarity coefficient (DSC). These metrics are defined as follows:

$$MAD = \frac{1}{n} \sum_{i=1}^n |A_i - F_i|, \quad (3)$$

$$RMSE = \frac{1}{n} \sqrt{\sum_{i=1}^n (A_i - F_i)^2}, \quad (4)$$

$$DSC = \frac{2|S_\alpha \cap S_m|}{(|S_\alpha| + |S_m|)}, \quad (5)$$

When comparing our RADP to conventional DP or manual segmentation,  $A_i$  represents the result of the conventional DP method, while  $F_i$  represents the result of RADP or manual segmentation. When comparing RADP to manual segmentation,  $A_i$  represents the result of RADP, while  $F_i$  represents the manual result. For these 3 different comparisons,  $S_\alpha$  and  $S_m$  denote the covering region of  $A_i$  and  $F_i$  respectively. The above metrics are calculated based on the detected airway lumen contour from each corresponding airway OCT B-scans.

## 4. Results

### 4.1. Segmentation results

To evaluate the segmentation performance, we compare our method to conventional DP algorithm [35] (denoted as Con. DP) and manual segmentation (denoted as Man. Seg.) results. As shown in Fig. 5 and Fig. 6, we used 2D airway OCT images in two different coordinate systems to enable a comparison between the results obtained by RADP and conventional DP.

As shown in the second and third columns of Fig. 5, where the detection results in yellow boxes have been magnified for observation, it is evident that conventional DP is sensitive to speckle noise and sheath artifacts, leading to inaccurate results. In contrast, our RADP is more precise in identifying the correct airway lumen contour by incorporating the sheath removal and adaptive region filtration steps.

In Fig. 6, we used polar coordinate images combined with 2D evaluation metrics to demonstrate the differences in accuracy among the three different segmentation results. We can find the superiority of RADP over conventional DP in terms of algorithm precision, as evidenced by the segmentation results and the MAD, RMSE, and DSC values. In all the exemplar images in Fig. 6, our RADP method has achieved the highest DSC scores, indicating the significant improvement introduced by the sheath removal and adaptive region filtration procedures.

Figure 7 shows the 3D reconstruction models without the anatomic bending operation. Both the airway lumen contours obtained by RADP and manual segmentation were tested without applying the IRAE correction. To compare these two methods more intuitively, we viewed the results from 6 different angles. As can be seen, our RADP can accurately reflect the real shape of airway lumen contour and its reconstruction result is highly similar with the result obtained by manual segmentation. The results in Fig. 7 demonstrate that RADP plays an important role in the later 3D reconstruction process.

In Table 2, the RMSE, MAD, and DSC values for three types of comparisons in Dataset1 and Dataset2 are shown. As can be seen, our RADP achieved greater robustness and more accurate results compared to the conventional DP. Specifically, our RADP reduces the mean MAD by 60.9%, the mean RMSE by 81.8%, and increases the mean DSC by 4.6%. These results are consistent with those obtained for Dataset2, where our RADP reduces the mean MAD by 63.3%, the mean RMSE by 77.8%, and increases the mean DSC by 3.5%. These results indicate that RADP is effective across different datasets.

**Table 2. Mean RMSE, MAD and DSC obtained from all images in Dataset1 and Dataset2**

Comparisons	Dataset1			Dataset2		
	MAD	RMSE	DSC	MAD	RMSE	DSC
Con. DP vs RADP	7.8306	20.2472	0.8802	9.4329	38.2613	0.9106
Con. DP vs Man. Seg.	8.1244	21.2753	0.8724	12.5738	35.3732	0.9013
RADP vs Man. Seg.	<b>3.1742</b>	<b>2.8816</b>	<b>0.9189</b>	<b>4.6204</b>	<b>7.8657</b>	<b>0.9327</b>



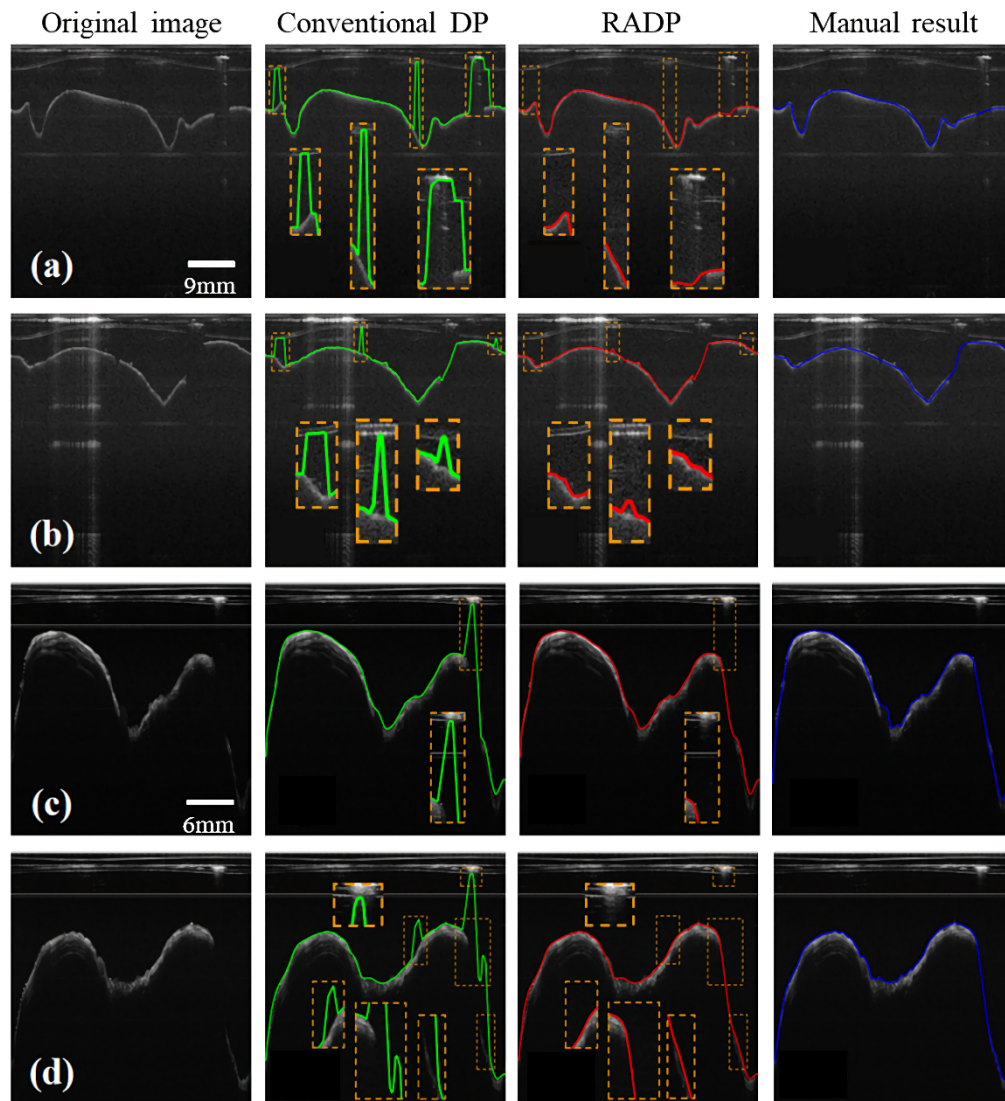


**Fig. 5.** Contrast display of the contour detection results of three different segmentation methods in the Cartesian coordinate system. The yellow boxes indicate the main differences between them. (a), (b) are images chosen from Dataset1, (c), (d) are images chosen from Dataset2.

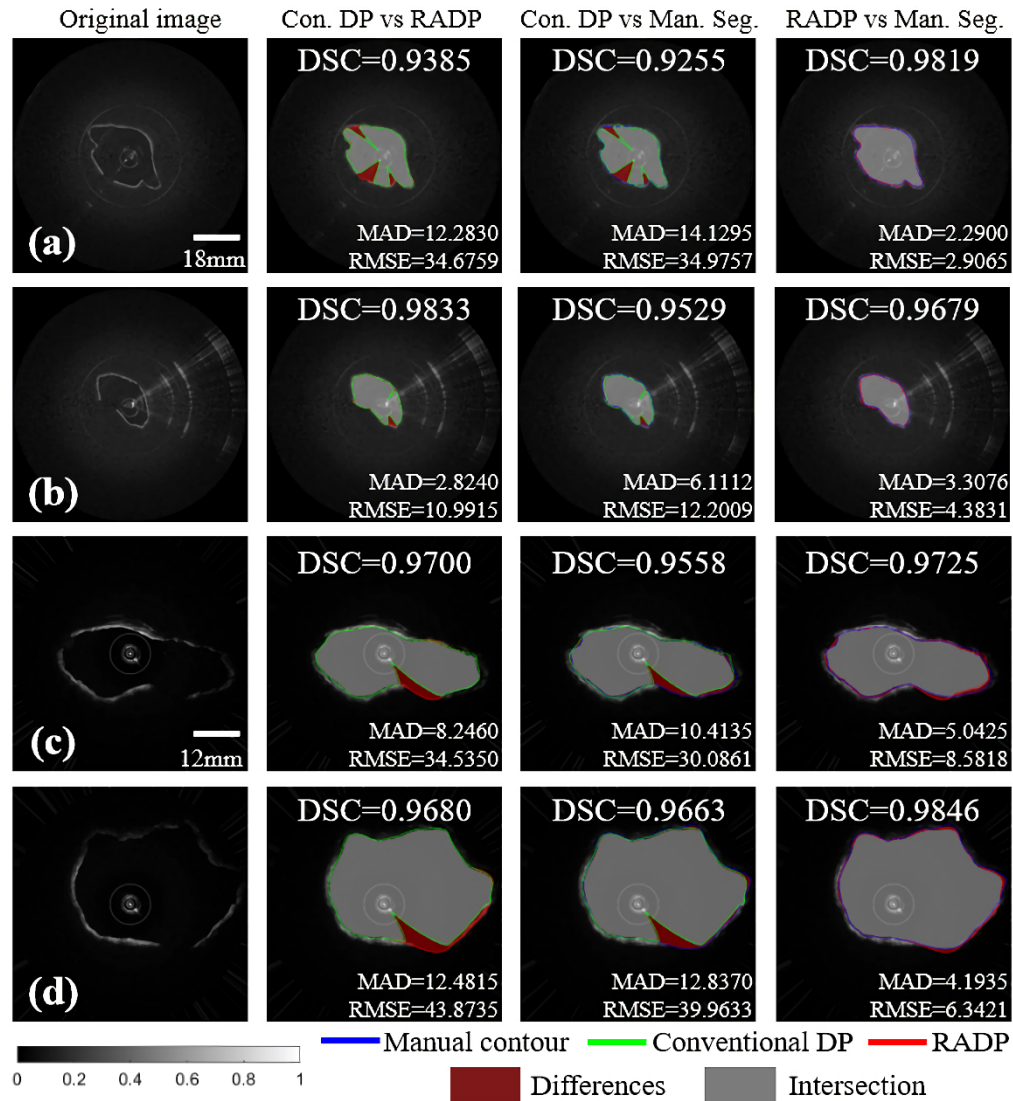


**Fig. 6.** Contrast display of the contour detection results using three different segmentation methods in the polar coordinate system. The red parts highlight the differences between these methods while the grey parts highlight the intersection between them. (a), (b) are images chosen from Dataset1, (c), (d) are images chosen from Dataset2.

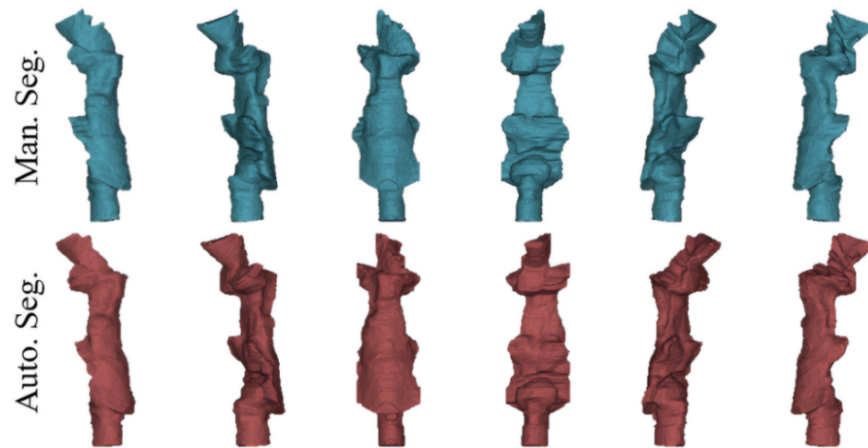


**Fig. 7.** The 3D reconstructed models of the upper airway, generated by our automatic segmentation method without IRAE correction, demonstrate its robustness and accuracy.

#### 4.2. 3D reconstruction results

We evaluate the results of 3D airway reconstruction obtained from 5 different combinations of processing methods: manual segmentation with manual IRAE correction, automatic segmentation with no IRAE correction, manual segmentation with automatic IRAE correction, automatic segmentation with manual IRAE correction, and automatic segmentation with automatic IRAE correction.

The 3D upper airway models are as shown in Fig. 8. The gold standard for comparison is the result of manual segmentation with manual IRAE correction. The differences between different segmentation methods or IRAE correction methods is highlighted by black arrows. In Fig. 8, the regions indicated by the red arrows demonstrate that the results generated without IRAE correction exhibit structural distortion, which significantly affects the morphological accuracy of the reconstructed results. Moreover, we can observe that the automatic IRAE correction method yields reconstruction results that are smoother than those obtained by the manual IRAE correction method, as indicated by the black arrows. Similarly, the automatic segmentation method has a similar effect as the manual segmentation method, and it improves the overall smoothness of the reconstruction results more significantly than the automatic IRAE correction method. From the observation of different complete 3D reconstruction results, it is noteworthy that compared with other results, the result obtained by our automatic segmentation method and automatic IRAE correction method has the highest similarity with the gold standard.

Furthermore, Fig. 9 shows the enlarged areas of the orange boxes in Fig. 8. As compared to the results obtained using the completely manual method shown in Fig. 9, it is evident that the reconstruction results obtained using our automatic segmentation method and automatic correction method are satisfactory in terms of both overall shape and detailed features. Meanwhile, as shown in Fig. 9, the highlighted exhibited structural distortion further demonstrate that IRAE correction is crucial to restore the anatomically correct upper airway structure. These results demonstrate that the combination of our automatic segmentation method, automatic IRAE correction method, and anatomic bending method can effectively and accurately reconstruct the upper airway structure.

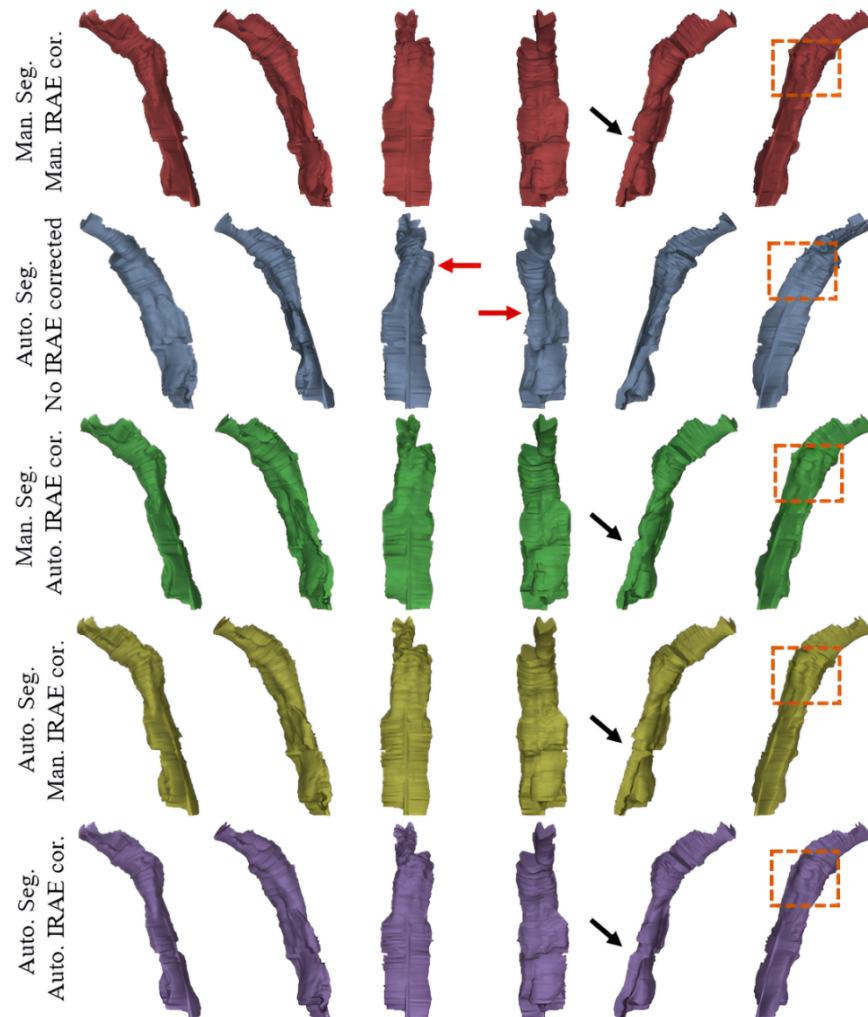


**Fig. 8.** The 3D reconstructed model of the upper airway was generated using five different combinations of contour segmentation and correction methods. Auto. Seg.: automatic segmentation with RADP; Man. Seg.: manual segmentation; IRAE Cor.: IRAE correction.

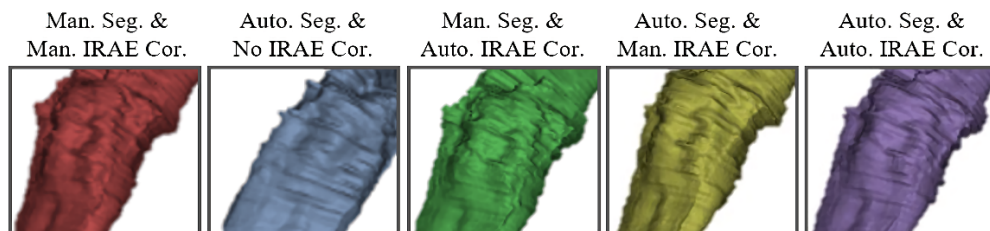


**Fig. 9.** The areas highlighted in the orange boxes of the 3D reconstruction results in Fig. 8.



### 4.3. Computational cost

The proposed algorithm was implemented in MATLAB, and was tested on a desktop computer with an Intel Core i5 processor and 32 GB of RAM. Table 4 summarizes the average processing time required by different methods for different datasets.

By analyzing the results presented in Table 3, it becomes evident that our method provides a considerable boost in efficiency when compared to the manual method, regardless of whether it is for a specific task (i.e., segmentation or IRAE correction) or for the complete reconstruction process. Specifically, in the processing of dataset1, our automatic segmentation, IRAE correction is about 3.4 times and 773.7 times faster than manual operations respectively. Automatic 3D reconstruction which includes the bending process is 4.7 times faster than manual reconstruction. For Dataset2, compared to manual processing, automatic segmentation is 4.7 times faster, and IRAE correction is 747.2 times faster. The overall 3D reconstruction procedure is 5.5 times faster than manual reconstruction, yet it takes longer than processing Dataset1 because the total number of images of Dataset2 is much larger.

**Table 3. Comparisons of average processing time for a complete dataset obtained by different methods**

Datasets	Segmentation		IRAE correction		3D reconstruction	
	Auto. Seg.	Man. Seg.	Auto. Cor.	Man. Cor.	Auto. Recon.	Man. Recon.
Dataset1	46.2 m	2.6 h	1.9 s	24.5 m	~50.1 m	~3.5 h
Dataset2	2.2 h	10.4 h	5.3 s	1.1 h	~2.4 h	~13.1 h

## 5. Discussion and conclusion

Our proposed method is a fully automatic 3D airway reconstruction method aims to reconstruct a complete and anatomically correct upper airway model from 2D OCT images. Our study represents an improvement over previous studies on airway OCT image processing which usually treat segmentation, image correction and 3D reconstruction as independent process. Our method effectively integrates these process in an automatic processing pipeline, resulting in a significant improvement in the overall image analysis efficiency.

Specifically, in our framework, the RADP segmentation method has achieved improved performance in terms of robustness to noise and artifact compared to previous DP-based algorithm. This is attributed to our specific image pre-processing operations including DP-based sheath removal, binarization and adaptive region filtration. Using the extracted airway lumen contour as input, the IRAE correction is performed to ensure that all detected 2D airway lumen contours are uniformly oriented, such that inaccurate 3D reconstruction is avoided. Finally, anatomic bending is employed to automatically and correctly restore the structure of the upper airway.

Despite the above advantages, the performance of our method is still affected by the Non-Uniform Rotation Distortion (NURD) of the imaging probe. The relative movement between the probe and the airway limits the accuracy of 3D reconstruction. In addition, during image pre-processing, the threshold  $q$  is determined empirically, and thus lacks flexibility. We hope to resolve this by introducing intensity-adaptive techniques in the future.

In conclusion, we have successfully demonstrated the feasibility and potential of a fully automatic 3D upper airway 3D reconstruction method. The reconstructed 3D upper airway structures obtained from our method exhibit a high degree of completeness and precision, and are comparable to those obtained from manual reconstruction. By using the proposed method, image analysis efficiency can be significantly improved, revealing its potential for future integration in airway OCT diagnosis systems.

**Funding.** Pearl River Talented Young Scholar Program of Guangdong Province (2017GC010282); Basic and Applied Basic Research Foundation of Guangdong Province (2021A1515012542, 2022A1515011748); Key-Area Research and Development Program of Guangdong Province (2018B030333001).

**Disclosures.** The authors declare that there are no conflicts of interest to this article.

**Data availability.** Data underlying the results presented in this paper are not publicly available at this time but may be obtained from the authors upon reasonable request.

## References

1. Z. Yaqoob, J. Wu, E. J. McDowell, X. Heng, and C. Yang, "Methods and application areas of endoscopic optical coherence tomography," *J. Biomed. Opt.* **11**(6), 063001 (2006).
2. B. E. Bouma, G. J. Tearney, H. Yabushita, M. Shishkov, C. R. Kauffman, D. DeJoseph Gauthier, B. D. MacNeill, S. L. Houser, H. T. Aretz, E. F. Halpern, and I. K. Jang, "Evaluation of intracoronary stenting by intravascular optical coherence tomography," *Heart* **89**(3), 317–320 (2003).
3. I. K. Jang, B. E. Bouma, D. H. Kang, S. J. Park, S. W. Park, K. B. Seung, K. B. Choi, M. Shishkov, K. Schlendorf, E. Pomerantsev, S. L. Houser, H. T. Aretz, and G. J. Tearney, "Visualization of coronary atherosclerotic plaques in patients using optical coherence tomography: comparison with intravascular ultrasound," *J. Am. Coll. Cardiol.* **39**(4), 604–609 (2002).
4. J. Yin, H. C. Yang, X. Li, J. Zhang, Q. Zhou, C. Hu, K. K. Shung, and Z. Chen, "Integrated intravascular optical coherence tomography ultrasound imaging system," *J. Biomed. Opt.* **15**(1), 010512 (2010).
5. B. J. Vakoc, M. Shishko, S. H. Yun, W. Y. Oh, M. J. Suter, A. E. Desjardins, J. A. Evans, N. S. Nishioka, G. J. Tearney, and B. E. Bouma, "Comprehensive esophageal microscopy by using optical frequency-domain imaging (with video)," *Gastrointest. Endosc.* **65**(6), 898–905 (2007).
6. M. J. Suter, B. J. Vakoc, P. S. Yachinski, M. Shishkov, G. Y. Lauwers, M. Mino-Kenudson, B. E. Bouma, N. S. Nishioka, and G. J. Tearney, "Comprehensive microscopy of the esophagus in human patients with optical frequency domain imaging," *Gastrointest. Endosc.* **68**(4), 745–753 (2008).
7. S. Lam, B. Standish, C. Baldwin, A. McWilliams, J. LeRiche, A. Gazdar, A. I. Vitkin, V. Yang, N. Ikeda, and C. MacAulay, "In vivo optical coherence tomography imaging of preinvasive bronchial lesions," *Clin. Cancer Res.* **14**(7), 2006–2011 (2008).
8. J. P. Williamson, R. A. McLaughlin, W. J. Noffsinger, A. L. James, V. A. Baker, A. Curatolo, J. J. Armstrong, A. Regli, K. L. Shepherd, G. B. Marks, D. D. Sampson, D. R. Hillman, and P. R. Eastwood, "Elastic properties of the central airways in obstructive lung diseases measured using anatomical optical coherence tomography," *Am. J. Respir. Crit. Care Med.* **183**(5), 612–619 (2011).
9. B. J. Wong, R. P. Jackson, S. Guo, J. M. Ridgway, U. Mahmood, J. Su, T. Y. Shibuya, R. L. Crumley, M. Gu, W. B. Armstrong, and Z. Chen, "In vivo optical coherence tomography of the human larynx: normative and benign pathology in 82 patients," *Laryngoscope* **115**(11), 1904–1911 (2005).
10. D. L. Traber, H. A. Linares, D. N. Herndon, and T. Prien, "The pathophysiology of inhalation injury—a review," *Burns* **14**(5), 357–364 (1988).
11. R. A. Cox, A. S. Burke, K. Soejima, K. Murakami, J. Katahira, L. D. Traber, D. N. Herndon, F. C. Schmalstieg, D. L. Traber, and H. K. Hawkins, "Airway obstruction in sheep with burn and smoke inhalation injuries," *Am. J. Respir. Cell Mol. Biol.* **29**(3), 295–302 (2003).
12. J. M. Ridgway, G. Ahuja, S. Guo, J. Su, U. Mahmood, Z. Chen, and B. Wong, "Imaging of the pediatric airway using optical coherence tomography," *Laryngoscope* **117**(12), 2206–2212 (2007).
13. M. Brenner, K. Kreuter, J. Ju, S. Mahon, L. Tseng, D. Mukai, T. Burney, S. Guo, J. Su, A. Tran, A. Batchinsky, L. C. Cancio, N. Narula, and Z. Chen, "In vivo optical coherence tomography detection of differences in regional large airway smoke inhalation induced injury in a rabbit model," *J. Biomed. Opt.* **13**(3), 034001 (2008).
14. J. C. Jing, L. Chou, E. Su, B. J. F. Wong, and Z. Chen, "Anatomically correct visualization of the human upper airway using a high-speed long range optical coherence tomography system with an integrated positioning sensor," *Sci. Rep.* **6**(1), 39443 (2016).
15. M. Mujat, R. Chan, B. Cense, B. Park, C. Joo, T. Akkin, T. Chen, and J. de Boer, "Retinal nerve fiber layer thickness map determined from optical coherence tomography images," *Opt. Express* **13**(23), 9480–9491 (2005).
16. M. A. Mayer, J. Hornegger, C. Y. Mardin, and R. P. Tornow, "Retinal nerve fiber layer segmentation on FD-OCT scans of normal subjects and glaucoma patients," *Biomed. Opt. Express* **1**(5), 1358–1383 (2010).
17. S. Farsiu, S. J. Chiu, J. A. Izatt, and C. A. Toth, "Fast detection and segmentation of Drusen in retinal optical coherence tomography images," in *Proceedings of Photonics West, Ophthalmic Technologies* (SPIE, 2008), pp. 1–12.
18. S. Niu, L. de Sistiernes, Q. Chen, T. Leng, and D. L. Rubin, "Automated geographic atrophy segmentation for SD-OCT images using region-based C-V model via local similarity factor," *Biomed. Opt. Express* **7**(2), 581–600 (2016).
19. J. Oliveira, S. Pereira, L. Gonçalves, M. Ferreira, and C. A. Silva, "Multi-surface segmentation of OCT images with AMD using sparse high order potentials," *Biomed. Opt. Express* **8**(1), 281–297 (2017).
20. D. Koozekanani, K. Boyer, and C. Roberts, "Retinal thickness measurements from optical coherence tomography using a Markov boundary model," *IEEE Trans. Med. Imaging* **20**(9), 900–916 (2001).
21. H. Ishikawa, D. M. Stein, G. Wollstein, S. Beaton, J. G. Fujimoto, and J. S. Schuman, "Macular segmentation with optical coherence tomography," *Invest. Ophthalmol. Visual Sci.* **46**(6), 2012–2017 (2005).



22. D. Zhu, Y. Shao, L. Leng, Z. Xu, J. Wang, F. Lu, and M. Shen, "Automatic biometry of the anterior segment during accommodation imaged by optical coherence tomography," *Eye Contact Lens* **40**(4), 232–238 (2014).
23. K.M. Kozłowski, G.K. Sharma, J. J. Chen, L. Qi, K. Osann, J. C. Jing, G.S. Ahuja, A.E. Heidari, P.S. Chung, S. Kim, Z. Chen, and B.J. Wong, "Dynamic programming and automated segmentation of optical coherence tomography images of the neonatal subglottis: enabling efficient diagnostics to manage subglottic stenosis," *J. Biomed. Opt.* **24**(09), 1 (2019).
24. N. Uribe-Patarroyo and B. E. Bouma, "Rotational distortion correction in endoscopic optical coherence tomography based on speckle decorrelation," *Opt. Lett.* **40**(23), 5518 (2015).
25. L. Qi, Z. Zhuang, S. Zhang, S. Huang, Q. Feng, and W. Chen, "Automatic correction of the initial rotation angle error improves 3D reconstruction in endoscopic airway optical coherence tomography," *Biomed. Opt. Express* **12**(12), 7616–7631 (2021).
26. L. Athanasiou, F. R. Nezami, M.Z. Galon, A. C. Lopes, P. A. Lemos, J.M. de la Torre Hernandez, E. Ben-Assa, and E.R. Edelman, "Optimized computer-aided segmentation and three-dimensional reconstruction using intracoronary optical coherence tomography," *IEEE J. Biomed. Health Inform.* **22**(4), 1168–1176 (2018).
27. H. Hautmann, A. Schneider, T. Pinkau, F. Peltz, and H. Geussner, "Electromagnetic catheter navigation during bronchoscopy: validation of a novel method by conventional fluoroscopy," *Chest* **128**(1), 382–387 (2005).
28. S. Krueger, H. Timinger, R. Grewer, and J. Borgert, "Modality-integrated magnetic catheter tracking for x-ray vascular interventions," *Phys. Med. Biol.* **50**(4), 581–597 (2005).
29. T. D. Nguyen, E. Su, J. F. Lazarow, F. C. Wheatley, A. Chin-Loy, A. Wang, D. Protsenko, G. S. Ahuja, Z. Chen, and B. J. Wong, "Constructing 3D models of the pediatric upper airway from long range optical coherence tomography images," in *Photonic Therapeutics and Diagnostics X* (SPIE, 2014), pp. 362–373.
30. R. Kafieh, H. Rabbani, and S. Kermani, "S, A review of algorithms for segmentation of optical coherence tomography from retina," *J. Med. Signals Sens.* **3**(1), 45 (2013).
31. J. Lo, T. T. Yu, D. Ma, P. Zang, J. P. Owen, Q. Zhang, R. K. Wang, M. F. Beg, A. Y. Lee, Y. Jia, and M. V. Sarunic, "Federated learning for microvasculature segmentation and diabetic retinopathy classification of OCT data," *Ophthalmol. Sci.* **1**(4), 100069 (2021).
32. A. Elsayy, G. Gregori, T. Eleiwa, M. Abdel-Mottaleb, and M. A. Shousha, "Pathological-corneas layer segmentation and thickness measurement in OCT images," *Transl. Vis. Sci. Technol.* **9**(11), 24 (2020).
33. L. Qi, K. Zheng, X. Li, Q. Feng, Z. Chen, and W. Chen, "Automatic three-dimensional segmentation of endoscopic airway OCT images," *Biomed. Opt. Express* **10**(2), 642–656 (2019).
34. L. Pan, F. Shi, D. Xiang, K. Yu, L. Duan, J. Zheng, and X. Chen, "OCTRexpert: a feature-based 3D registration method for retinal OCT images," *IEEE Trans. Image Process.* **29**, 3885–3897 (2020).
35. L. Qi, S. Huang, A. E. Heidari, C. Dai, J. Zhu, X. Zhang, and Z. Chen, "Automatic airway wall segmentation and thickness measurement for long-range optical coherence tomography images," *Opt. Express* **23**(26), 33992–34006 (2015).
36. J. Jing, J. Zhang, A. C. Loy, B. J. Wong, and Z. Chen, "High-speed upper-airway imaging using full-range optical coherence tomography," *J. Biomed. Opt.* **17**(11), 110507 (2012).